

Experimental and Numerical Study of Electroporation Induced by Long Monopolar and Short Bipolar Pulses on Realistic 3D Irregularly Shaped Cells

Michele A. Chiapperino, Luciano Mescia¹, Pietro Bia², Barbara Starešinič³, Maja Čemažar⁴, Vitalij Novickij⁵, Aleksandr Tabašnikov, Stewart Smith⁶, Janja Dermol-Černe⁷, and Damijan Miklavčič⁸

Abstract—In this article, the reversible electroporation induced by rectangular long unipolar and short bipolar voltage pulses on 3D cells is studied. The cell geometry was reconstructed from 3D images of real cells obtained using the confocal microscopy technique. A numerical model based on the Maxwell and the asymptotic Smoluchowski equations has been developed to calculate the induced transmembrane voltage and pore density on the plasma membrane of real cells exposed to the pulsed electric field. Moreover, in the case of the high-frequency pulses, the dielectric dispersion of plasma membranes has been taken into account using the second-order Debye-based relationship. Several numerical simulations were performed and we obtained suitable agreement between the numerical and experimental results.

Index Terms—Electropermeabilization, multicellular systems, pulsed electric field, electromagnetic modeling, 3D geometry reconstruction, dielectric dispersion.

Manuscript received September 24, 2019; revised December 17, 2019 and January 20, 2020; accepted January 23, 2020. Date of publication February 3, 2020; date of current version September 18, 2020. The work was supported in part by the bando “INNONETWORK-sostegno alle attività di R&S per lo sviluppo di nuove tecnologie sostenibili, di nuovi prodotti e servizi,” plan: T-CARE- Teleassistenza e monitoraggio innovativi dei parametri vitali a domicilio con biosensori indossabili, Project B37H17005210007, in part by the Slovenian Research Agency (ARRS) research core funding P2-0249 and IP-0510, and in part by the Research Council of Lithuania under Grant S-MIP-19-13. (Corresponding author: Luciano Mescia.)

M. A. Chiapperino is with the Department of Electrical and Information Engineering, Politecnico di Bari.

L. Mescia is with the Department of Electrical and Information Engineering, Politecnico di Bari, 70125 Bari, Italy (e-mail: luciano.mescia@poliba.it).

P. Bia is with Elettronica S.p.A., Design Solution Department.

B. Starešinič and M. Čemažar are with the Department of Experimental Oncology, Institute of Oncology Ljubljana.

V. Novickij is with the Faculty of Electronics, Vilnius Gediminas Technical University.

A. Tabašnikov is with the Institute for Micro and Nano Systems, School of Engineering, The University of Edinburgh.

S. Smith is with the Institute for Bioengineering, School of Engineering, The University of Edinburgh.

J. Dermol-Černe and D. Miklavčič are with the Faculty of Electrical Engineering, University of Ljubljana.

Digital Object Identifier 10.1109/TBME.2020.2971138

I. INTRODUCTION

THE CELL membrane is an essential biological structure that controls the molecular flow between the “cell inside,” i.e. intracellular and “cell outside,” i.e. extracellular environment. When the cell is exposed to a pulsed electric field, the membranes become permeable, which promotes the molecular exchange between the inside and outside of the cell. This non-thermal electric process is called electroporation (EP) [1]. Depending on the intensity and duration of the applied electric field, the EP process can be reversible or irreversible. In medical applications, reversible electroporation is used to introduce chemotherapeutic drugs in electrochemotherapy (ECT) or plasmids in gene electrotransfer into cells, whereas irreversible electroporation (IRE) is used to kill cancer cells and to obtain the consequent tumor ablation [2]. Moreover, IRE is an emerging tool for catheter-based cardiac ablation [3].

In IRE and ECT, high voltage electrical pulses on the timescale of several tens of microseconds are applied. IRE and ECT are easy to apply and they are not affected by local blood flow. Moreover, they don't produce any collateral damage to anatomical borders or result in thermal damage, because they don't induce protein denaturation [4]. In contrast, the strong electric fields and pulse duration used in IRE and ECT generate muscle contractions and pain, thus, anesthesia and muscle relaxants are required during treatment. To mitigate these drawbacks, high-frequency irreversible electroporation (HF-IRE) is introduced. HF-IRE utilizes high-frequency short bipolar pulses with a repetition rate exceeding the frequency of tetanic contractions [5]. Recently, high-frequency short bipolar pulses were also applied to achieve reversible electroporation, for example, to introduce fluorescent dye into cells [6] and the chemotherapeutic drug cisplatin in electrochemotherapy, i.e. high-frequency electroporation (HF-EP) [7]. In our work, we applied similar pulses as in the HF-EP study.

Since the basic mechanisms of the EP process have not yet been fully clarified, different mathematical models of EP have been proposed in the literature to study pore formation in biological membranes [8], [9]. Major limitations of such models are due to the various approximations pertaining to the stationary dielectric properties and simple cell shapes.

As a result, errors in estimating the parameters characterizing the EP process can occur. Different papers demonstrate the influence of the irregular shape of the cell membrane on the EP process [10]–[13]. They have some weaknesses which keep the models from being powerful. To carry out a predictive analysis of the experimental results, two-dimensional (2D) numerical models have been developed [14]. However, the 2D model environment is significantly different from the 3D one since cells are treated as infinitely long columns. Also, the interinfluence of pore density on different parts of the cell membrane is neglected. More realistic three-dimensional (3D) models have been presented [13], [15], [16], but the cell dielectric properties are considered frequency-independent. Furthermore, multiple cell models based on canonical [17] or 2D [6], [18], and 3D [19] irregular cell shapes have been proposed in the literature with the aim to provide a predictive description of the EP effects of each cell on its neighbors. The purpose of this paper is to analyze and compare the reversible EP induced by longer monopolar and high-frequency pulses on 3D irregularly shaped cells from both experimental and numerical points of view. By using confocal microscopy, realistic cell shapes, as well as the time course of calcium influx after EP, have been acquired. The realistic cell shapes were extracted from the z-stack and imported into the computational environment. In accordance with the asymptotic EP model based on the Smoluchowski partial differential equation [8], the nonlinear effect due to the pore formation has been taken into account. Moreover, for shorter bipolar pulses, the dispersive properties of the cell membrane have been modeled by using a second-order Debye-based relationship. The developed numerical algorithm simultaneously solves the Maxwell equations, the Smoluchowski partial differential equation, and the differential equation relating the electric and polarization fields. In this way, a good agreement between the numerical and experimental results was obtained. To the best of our knowledge, the proposed study is the first in which a 3D numerical model of EP involving realistic cell shapes, as obtained by confocal microscopy and characterized by dispersive dielectric properties, was created and validated with experimental results of calcium uptake after EP. Our study paves the way to more realistic modeling of EP phenomena.

II. MATERIAL AND METHODS

A. Cell Preparation, Imaging, and Pulse Application

One day before our experiments, the mouse melanoma cell line B16-F10 (ATCC CRL-6475, LGC, Teddington, UK) stably transfected with the fluorescent protein tdTomato was grown on glass electrode slides (see Fig. 1(a)) in a humidified atmosphere at 37 °C and 5% CO₂ in the culture medium Advanced Minimum Essential Medium (AMEM, Gibco, Thermo Fischer Scientific, USA). The emitted red light that is caused by the fluorescent protein tdTomato in the cytoplasm enables cell observation without any additional dyes. A culture medium was supplemented with a 5% fetal bovine serum (FBS, Gibco, Thermo Fisher Scientific), L-alanine-L-glutamine (GlutaMAX, Gibco, Thermo Fisher Scientific), and gentamycin antibiotics (Krka, Novo mesto, Slovenia), and penicillin (Grünenthal, Aachen,

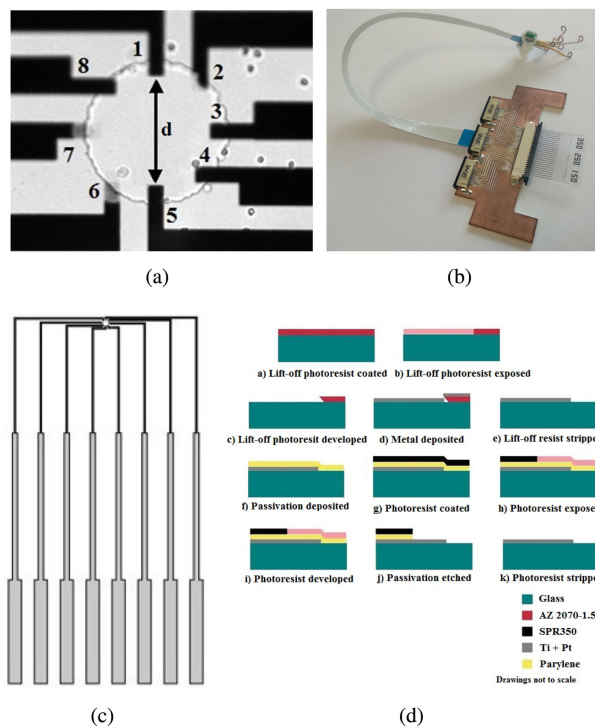


Fig. 1. Microelectrodes system used in the experiments: (a) magnified image of the electrodes used in the experiments in correspondence of the positioning zone of the chamber holding the biological cells. The distance between the electrodes 1 and 5 is $d = 250 \mu\text{m}$; (b) a custom-made holder used to connect the electrodes to the pulse generator; (c) a geometrical scheme; and (d) procedure of microelectrodes making.

Germany). Electroporation was detected using the dye Fluo-4 AM (Thermo Fischer Scientific). The Fluo-4 AM is a cell-permeable calcium-sensitive dye which is cleaved inside cells to cell-impermeable Fluo-4, and exhibits an increase in fluorescence upon the binding calcium. The intracellular calcium concentration in the cell culture medium was 1.8 mM, which is considerably higher than the cytosolic calcium concentration (around 100 nM). Thus, after electroporation, calcium entered into the cells predominantly from the culture medium, and caused an increase of the Fluo-4 signal. On the day of our experiments, the culture medium was first changed to a culture medium containing 4 M Fluo-4 AM, and the cells were incubated for 30 min in a humidified atmosphere at 37 °C and 5% CO₂ to allow for dye loading. After 30 min, the medium with the dye was changed to a dye-free culture medium, and the sample was left in an incubator for an additional 30 min to allow for the completion de-esterification of the intracellular AM esters before starting the experiments. Cells stably transfected with the fluorescent protein tdTomato, which emitted fluorescence in the red range, and in the green range from the Fluo-4 AM when the intracellular calcium concentration increased due to the membrane EP. Right before the experiments, the glass electrode slides were mounted under the microscope on a custom-made connector (see Fig. 1(b)). The ZEISS LSM 800 confocal laser scanning microscope equipped with a water immersion objective W Plan-Apocromat 20 × 1.0 DIC (Zeiss, Germany) was used for cell imaging. Two lasers were used for excitation, at 561 nm

(red signal) and 488 nm (green signal). Both signals were acquired for each slice/time-point. First, the z-stack was acquired with a spacing of $0.5 \mu\text{m}$ between slices to obtain a 3D image of the cells in the area between the electrodes. Then, a z-plane in the middle of the z-stack was selected, and a time-lapse of electroporated cells was acquired with a 4 s interval between frames for a duration of 90 s. Pulses were delivered after 12 s (i.e. three frames).

B. Electrode Fabrication and Electric Field Delivery

Three-inch glass wafers were first treated in an oxygen plasma barrel asher for 60 min to make sure that the surface was not contaminated. After that, the wafers were primed for 10 min in HMDS vapour to increase the photoresist adhesion. The wafers were then covered with an AZ nLOF 2070-1.5 lift-off resist by spin coating using a manual spinner for 45 seconds at 3000 RPM to produce a $1.5 \mu\text{m}$ resist thickness. After soft baking at 100°C for 90 s, the resist was exposed with the electrode pattern for 20 seconds in a Suss MA8 mask aligner and then baked at 115°C for 60 s. The resist was a dish developed for 90 seconds in an AZ 726 MIF developer, and the wafers were washed in DI water and dried using a nitrogen gun. A descum process was performed in the oxygen plasma barrel asher for 2.5 min to remove residual photoresist in developed trenches. The wafers were covered with 100 nm thick platinum in an electron beam evaporator (ANS) with 10 nm thick titanium underneath as an adhesion layer. Metal lift-off was performed in a Petri dish using a MP 1165 resist remover and ultrasonic agitation at 50°C for 15 min. The wafers were then soaked in IPA at 50°C for 2 min, rinsed using IPA and DI water, and finally dried. Before we covered the wafers with a passivation layer, they were treated again in the oxygen plasma barrel asher for 5 min to promote adhesion. The wafers were coated with Parylene C (an average measured thickness of 937 nm) using a SCS Labcoter 2 tool. Parylene C was used because it is known to be biocompatible [20]. The wafers were coated with $2.2 \mu\text{m}$ thick SPR350 resist using a SVG track and resist was exposed for 15 s in the mask aligner. The resist was developed using the SVG track, and then oxygen plasma etched (49 sccm O_2 , 50 mTorr , 100 W) for 12 min using JLS RIE80 to open the electrodes. The wafers were finally coated with a $1.5 \mu\text{m}$ thick SPR350 resist using a SVG track and diced to produce chips. The remaining photoresist was removed from the chips using acetone in a Petri dish at 50°C for 10 min. The chips were soaked in IPA at 50°C for 2 min, rinsed using IPA and DI water, and dried. Finally, the chips were exposed to the aforementioned O_2 plasma etch process for 30 s, which is expected to remove around 50 nm of Parylene, and to make its surface hydrophilic [21]. The macro geometry of the electrodes is seen in Fig. 1(c). Moreover, Fig. 1(d) shows the scheme of the procedure for making the microelectrodes. The chamber where cells were growing is shown in Fig. 1(a), as seen under the microscope. In the simulation as well as in the experiments, voltage was only applied to electrodes 1 and 5 (see Fig. 1), and the distance between them was $250 \mu\text{m}$. The electrodes were connected to the pulse generator with a custom-made holder (Fig. 1(b)). The thickness of each electrode was 100 nm, and so

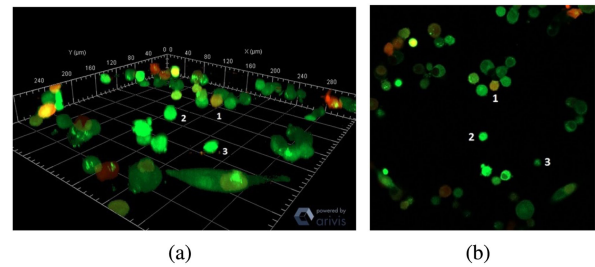


Fig. 2. The acquired field of view between the electrodes before electroporation: (a) a 3D view of cells obtained using the ZEN software suite; and (b) a cross-section of the reconstructed cells. Red: tdTomato, green: Fluo-4.

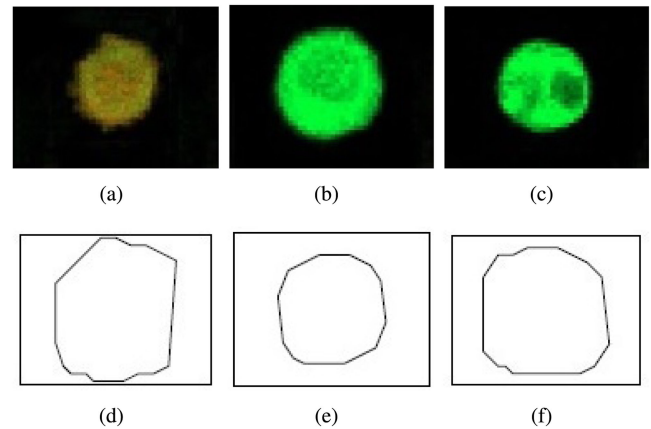


Fig. 3. Cross-sections of (a) cell 1, (b) cell 2, and (c) cell 3 at $z = 8 \mu\text{m}$, and (d)–(f) corresponding contour plots.

they were quite resistive as the path for the electric current was relatively narrow. For the application of monopolar pulses, the BetaTech generator B10 (Electro cell B10, BetaTech, France) was used, and eight pulses of $100 \mu\text{s}$ at repetition frequency 1 Hz, with a range of voltage from 60 V to 120 V in steps of 20 V, were applied.

C. Image Processing and 3D Cells Geometry Reconstruction

Fig. 2 shows the images of the real cells used during the experiments. In particular, to reduce the computational efforts, only the three cells labeled with “1,” “2,” and “3” have been considered. The RGB images of the cells’ z-stack have been analyzed using a MATLAB extraction algorithm based on the Sobel method for edge detection [22]. The algorithm has good performance in terms of edge detection, reduced numerical complexity, and low sensitivity to noise. The Sobel operator is based on convolving the image with a small, separable, and integer-valued filter in the horizontal and vertical directions. In the 3D reconstruction, the cross-sections of the cells have been considered every eight images; thus in a vertical increment of $4 \mu\text{m}$ from the bottom to the top of the cells. The extraction process generates the vector image of the contour of each cell for different z-sections (see Fig. 3(d)–(f)). First, the algorithm acquires the RGB image and converts it to gray scale. Then,

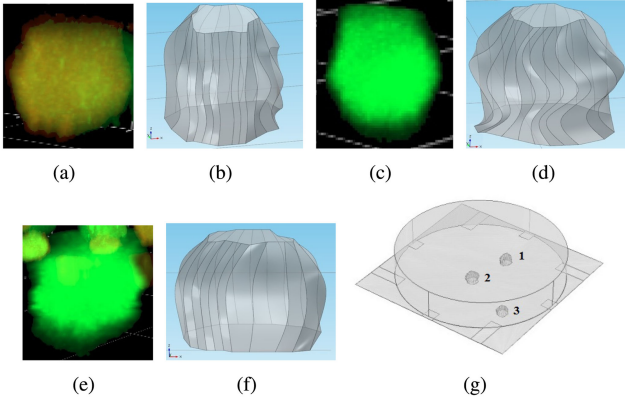


Fig. 4. ZEN software 3D view of (a) cell 1, (c) cell 2, and (e) cell 3. Red: tdTomato, green: Fluo-4. Reconstructed 3D geometry of (b) cell 1, (d) cell 2, and (f) cell 3. (g). Position of cells 1, 2, and 3 with respect to the electrodes.

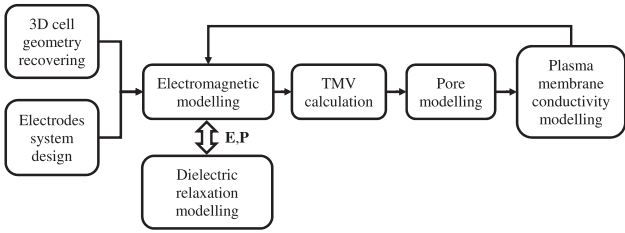


Fig. 5. Block diagram of the developed Multiphysics numerical model.

the edge detection is performed using the standard Sobel operator method in which a fudge factor $FF = 0.7$ was used as a parameter. The resulting image is vertically and horizontally stretched by an integer factor DF ranging from 2 to 7. The interior spaces were filled and the objects connected on the edges were removed using a connectivity factor $CF = 1$. The objects were smoothed using a flat diamond-shaped structuring element characterized by an integer factor SF ranging from 1 to 2. Finally, the three-dimensional geometry of each cell was reconstructed from the computed vector images of each z-stack using the Loft operator of COMSOL Multiphysics software. The generated 3D cell shapes were validated comparing them to the corresponding ones reported in the ZEN software (Fig. 4). Fig. 4(g) shows the 3D system model consisting of the terminal parts of the electrodes, the extracellular medium represented by the cylinder in the center figure, and the biological cells.

III. THEORETICAL MODEL

Fig. 5 illustrates the block diagram of the developed Multiphysics model. At a quick glance, it is clear that the design of the whole electrode system, as well as the 3D reconstruction of the biological cells, are essential steps for electromagnetic modeling. Moreover, it is worthwhile to note the coupling between the electromagnetic and the EP phenomena. In fact, the pore density changes the membrane conductivity, which as a result, modifies the spatial and temporal distribution of the electric field inside all cell compartments. The simulations were performed using the software Comsol Multiphysics 5.0 (Comsol AB, Stockholm, Sweden).

The electromagnetic analysis is based on the Maxwell equations:

$$\oint_{\Gamma} \mathbf{H} \cdot d\mathbf{l} = \int_S \left(\sigma \mathbf{E} + \epsilon_0 \frac{\partial \mathbf{E}}{\partial t} + \frac{\partial \mathbf{P}}{\partial t} \right) \cdot d\mathbf{S} \quad (1)$$

$$\oint_{\Gamma} \mathbf{E} \cdot d\mathbf{l} = -\frac{\partial}{\partial t} \int_S \mathbf{B} \cdot d\mathbf{S} \quad (2)$$

where \mathbf{E} and \mathbf{H} are the electric and magnetic field, respectively, \mathbf{B} is the magnetic flux density, and \mathbf{P} is the electric polarization field. In particular, taking into account the small cell size and the micro second electric pulses, the time variation of the magnetic flux can be neglected. As a result, equations (1)–(2) can be simplified into:

$$\nabla \cdot \left(\epsilon_0 \frac{\partial \nabla \phi}{\partial t} + \sigma \nabla \phi - \frac{\partial \mathbf{P}}{\partial t} \right) = 0 \quad (3)$$

$$\mathbf{E} = -\nabla \phi \quad (4)$$

where ϕ is the electric potential. The transmembrane voltage (TMV) can be calculated as:

$$\text{TMV} = \phi_i - \phi_o \quad (5)$$

where ϕ_i and ϕ_o are the electric potentials on the inner and outer sides of the plasma membranes, respectively. A dispersive modeling of the interaction between the electric fields and the plasma membrane medium was taken into account, too. In particular, from a macroscopic point of view, the second-order Debye relationship was used to model the dielectric relaxation of the plasma membranes [23], [24]:

$$\epsilon_{Pm}(\omega) = \epsilon_{\infty} + \frac{\Delta \epsilon_{1,Pm}}{1 + j\omega\tau_{1,Pm}} + \frac{\Delta \epsilon_{2,Pm}}{1 + j\omega\tau_{2,Pm}} \quad (6)$$

where ϵ_{∞} is the high-frequency permittivity, $\Delta \epsilon_{1,Pm}$ and $\Delta \epsilon_{2,Pm}$ are the first and the second plasma membrane relaxation amplitudes, respectively, and $\tau_{1,Pm}$ and $\tau_{2,Pm}$ are the first and the second plasma membrane relaxation times, respectively. Applying the inverse Fourier transform to equation (6), the following time-domain partial differential equation linking the electric polarization field with the electric field can be obtained:

$$a_2 \frac{\partial^2 \mathbf{P}_{Pm}}{\partial t^2} + a_1 \frac{\partial \mathbf{P}_{Pm}}{\partial t} + \mathbf{P}_{Pm} = b_2 \frac{\partial^2 \mathbf{E}}{\partial t^2} + b_1 \frac{\partial \mathbf{E}}{\partial t} + b_0 \mathbf{E} \quad (7)$$

where

$$a_1 = \tau_{1,Pm} + \tau_{2,Pm} \quad (8)$$

$$a_2 = \tau_{1,Pm} \tau_{2,Pm} \quad (9)$$

$$b_0 = \Delta \epsilon_{1,Pm} + \Delta \epsilon_{2,Pm} + \epsilon_{\infty} - \epsilon_0 \quad (10)$$

$$b_1 = (\Delta \epsilon_{2,Pm} + \epsilon_{\infty} - \epsilon_0) \tau_{1,Pm} + (\Delta \epsilon_{1,Pm} + \epsilon_{\infty} - \epsilon_0) \tau_{2,Pm} \quad (11)$$

$$b_2 = (\epsilon_{\infty} - \epsilon_0) \tau_{1,Pm} \tau_{2,Pm} \quad (12)$$

The developed model has considerable complexity since it takes into account the actual electrodes geometry and the irregular cell shape, as well as the dielectric relaxation of the cell media. Thus, to reduce the computational efforts and to solve some convergence problems, the thin plasma membrane was replaced with a distributed impedance boundary condition [6],

[16], [19]. In particular, considering the dispersive dielectric response of the plasma membrane medium, a more general boundary condition was derived and numerically implemented. In detail, the following equation can be derived:

$$J = \frac{\sigma_{Pm}}{h} \text{TMV} + \frac{\epsilon_0 \epsilon_{Pm}}{h} \frac{\partial \text{TMV}}{\partial t} \quad (13)$$

where J is the current density at the interface between the extracellular medium and the cytoplasm, ϵ_0 is the permittivity of free space, and σ_{Pm} and h are the plasma membrane conductivity thickness, respectively. Moreover, the time-dependent plasma membrane permittivity, ϵ_{Pm} , was evaluated using the equation:

$$\epsilon_{Pm} \mathbf{E} = \mathbf{P} + \epsilon_0 \mathbf{E} \quad (14)$$

where $\mathbf{E} = \nabla \phi$ and \mathbf{P} is the solution of the equation (7). By solving equations (3)–(4) in conjunction with equations (7)–(14), the space-time dependence of the TMV can be calculated. This TMV directly drives the temporal evolution of plasma membrane pore density N . In particular, the biophysical behavior was modeled by using the asymptotic Smoluchowski first-order partial differential equation [25]:

$$\frac{\partial N}{\partial t} = \alpha \left[\exp\left(\frac{\text{TMV}}{V_{ep}}\right)^2 - \frac{N}{N_0} \right] \quad (15)$$

where α is the pore creation rate density coefficient, V_{ep} is the characteristic voltage of EP, and N_0 is the pore density at rest. Assuming that both the pore radius and the conductivity inside the pore are constant, the membranes conductivity is given by:

$$\sigma_{Pm} = \sigma_0 + \pi r_p^2 N \sigma_p \Gamma_{Pm} \quad (16)$$

where σ_0 is the static plasma membrane conductivity at rest, r_p is the pore radius, σ_p is the conductivity of the solution inside the pore, and Γ_{Pm} is calculated using the following equation:

$$\Gamma_{Pm} = \frac{e^{\nu_{Pm}} - 1}{\frac{w_0 e^{w_0 - \eta \nu_{Pm}} - \eta \nu_{Pm} e^{\nu_{Pm}}}{w_0 - \eta \nu_{Pm}} - \frac{w_0 e^{w_0 + \eta \nu_{Pm}} + \eta \nu_{Pm}}{w_0 + \eta \nu_{Pm}}} \quad (17)$$

In equation (17), w_0 is the pore energy barrier, η is the relative entrance length of pores, and ν_{Pm} is the non-dimensional TMV for the plasma membrane evaluated as:

$$\nu_{Pm} = \frac{q_e \text{TMV}}{kT} \quad (18)$$

A rectangular electric pulse was applied as a boundary condition $V = V_0$ to electrode 1 and 5. In our computations, the computational window in the time domain was partitioned into sub-intervals in which the PARDISO and MUMPS solvers were properly applied. The meshing was refined until 58 nm. The geometric, electric, and EP parameters used in the numerical algorithm are summarized in Table I.

IV. RESULTS AND DISCUSSION

A. Exposure to Longer Monopolar Pulses

The developed numerical model was first tested on irregular 3D cells (“1,” “2,” and “3”) exposed to rectangular monopolar 100 μs long pulses. Fig. 6 illustrates the computed electric field

TABLE I
ELECTRICAL, GEOMETRICAL, AND ELECTROPORATION PARAMETERS

Symbol	Value	Description
$\tau_{1,Pm}$	3×10^{-9} s	First relaxation time of membrane [26]
$\tau_{2,Pm}$	4.6×10^{-10} s	Second relaxation time of membrane [26]
$\Delta \epsilon_{1,Pm}$	2.3×10^{-11} Fm ⁻¹	First relaxation amplitude of membrane [26]
$\Delta \epsilon_{2,Pm}$	7.4×10^{-12} Fm ⁻¹	Second relaxation amplitude of membrane [26]
ϵ_∞	13.9×10^{-12} Fm ⁻¹	High frequency permittivity [8]
ϵ_0	8.85×10^{-12} Fm ⁻¹	Dielectric permittivity of vacuum
ϵ_{er}^{Ex}	72	Relative permittivity of extracellular medium [8]
ϵ_0^{Pm}	5	Static relative permittivity of membrane [8]
ϵ_r^{Cp}	72	Relative permittivity of cytoplasm [8]
σ_{Ex}	1.2 Sm ⁻¹	Conductivity of the extracellular medium [8]
σ_0^{Pm}	9.5×10^{-9} Sm ⁻¹	Passive conductivity of the membrane [8]
σ_{Cp}	0.3 Sm ⁻¹	Conductivity of cytoplasm [8]
σ_p	1.2 Sm ⁻¹	Conductivity of the solution inside the pore [8]
r_p	0.8 nm	Pore radius [8]
α	1×10^9 m ⁻² s ⁻¹	Pore creation rate density [8]
V_{ep}	224 mV	Characteristic voltage of electroporation [8]
$N_{e,q}$	3.3×10^6 m ⁻²	Equilibrium pore density [8]
w_0	3.2	Energy barrier inside the pore [8]
η	0.15	Relative length of pore entrance area [8]
q_e	$1.65e - 19$ C	Electron electric charge
k	1.38×10^{-23} JK ⁻¹	Boltzmann constant
T	295 K	Temperature
t	5 nm	Membrane thickness [27]

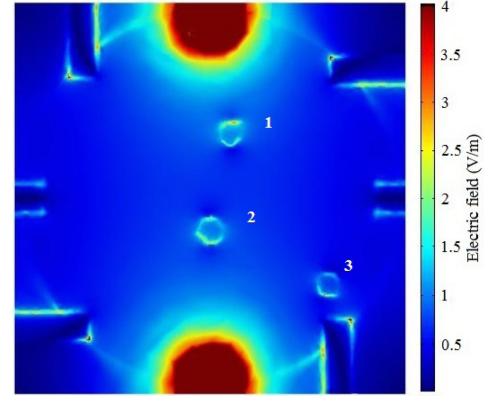


Fig. 6. Electric field distribution on the microelectrodes plane ($z = 0$) at the time instant $t_0 = 100 \mu\text{s}$.

distribution on the microelectrodes plane when electrodes 1 and 5 are driven by a pulse having amplitude 60 V, a delay time $T_d = 5 \mu\text{s}$, and rise and fall times 0.1 μs . It can be noticed that the microelectrodes system used in the experiment produces an inhomogeneous electric field around the cells exhibiting “hot spots” on the cell membranes. This electric field distribution is an important issue to take into account since it directly drives the electroporation phenomenon. Figs. 7(a) and 7(b) show the temporal evolution of TMV and pore density calculated at the points where the pore density exhibits its maximum value. The frequency spectrum of the pulse has the first zero at the frequency $f_0 = 1/\tau_s$, where τ_s is the signal duration. Thus, the energy of the pulse having duration $\tau_s = 100 \mu\text{s}$ is mainly contained within the frequency range 10 kHz wide, where the electrical

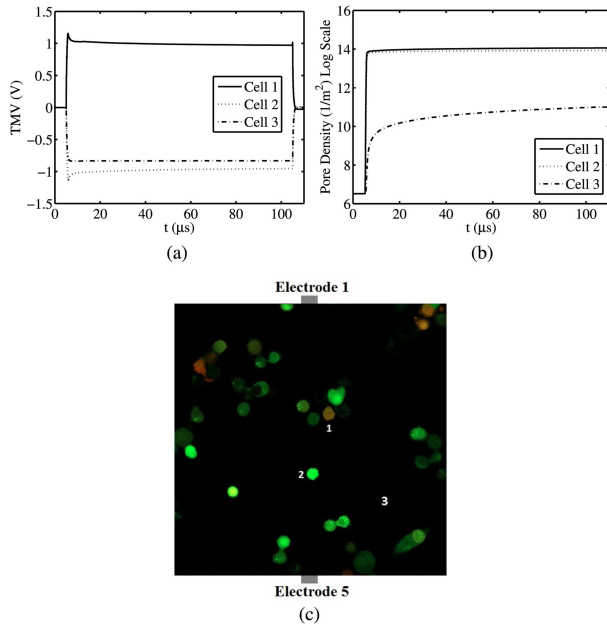


Fig. 7. Temporal evolution of (a) TMV and (b) pore density corresponding to the point where the pore density had its maximum value, and (c) Experimental results. Rectangular unipolar pulse, voltage amplitude 60 V, duration $T = 100 \mu\text{s}$, delay time $T_d = 5 \mu\text{s}$, rise time $t_r = 0.1 \mu\text{s}$, fall time $t_f = 0.1 \mu\text{s}$. Red: tdTomato, green: Fluo-4.

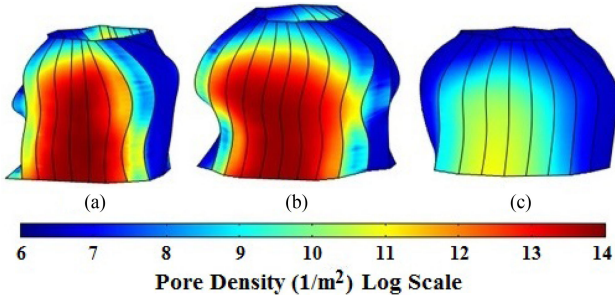


Fig. 8. Pore density of the plasma membrane surface for (a) cell 1, (b) cell 2, and (c) cell 3 at time instant $t_0 = 110 \mu\text{s}$. Rectangular unipolar pulse, voltage amplitude 60 V, duration $T = 100 \mu\text{s}$, rise time $t_r = 0.1 \mu\text{s}$, fall time $t_f = 0.1 \mu\text{s}$.

properties of the cell media can be considered frequency independent. As a result, in the developed numerical model, the dispersive behavior was neglected [12]. The application of the external rectangular unipolar pulse generates a rapid increase of the TMV, which reaches maximal values of about 1.1 V, and -1.1 V and -0.8 V for cells 1, 2, and 3, respectively (see Fig. 7(a)). Then, the growing of pore density adds additional pathways for current to cross the membrane which generates a fast increase of the membrane conductivity. As a result, a decrease in the TMV occurs. The obtained numerical results were compared to experimental ones reported in Fig. 7(c). By inspection of Figs. 7(b) and 7(c), it can be seen that cell 1 and cell 2 are both electroporated, whereas cell 3 is not electroporated. Thus, the agreement between the numerical and experimental results can be inferred. Furthermore, Fig. 8 shows surface distribution of the pore density for the three cells at the time instant $t_0 = 110 \mu\text{s}$. Considering that in the asymptotic pore model the pores reseal in the time range of seconds, the pore

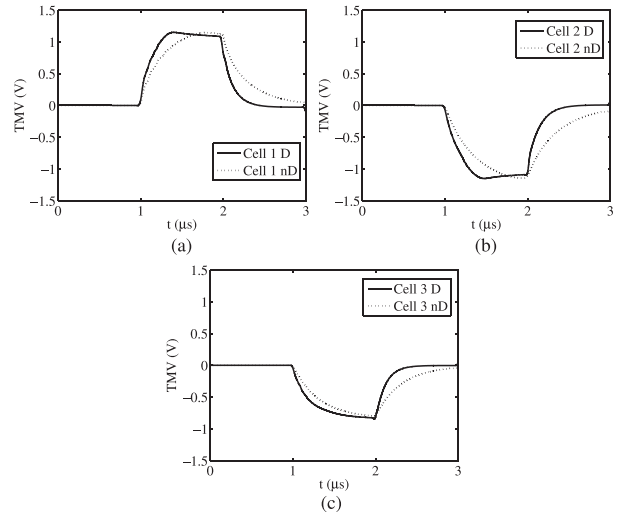


Fig. 9. Temporal evolution of TMV for (a) cell 1, (b) cell 2, and (c) cell 3 obtained using the dispersive (D) and non-dispersive (nD) model. Positive part of the bipolar pulse, voltage amplitude 60 V, pulse duration $T_p = 1 \mu\text{s}$, delay time $T_d = 1 \mu\text{s}$, rise time $t_r = 0.1 \mu\text{s}$, and fall time $t_f = 0.1 \mu\text{s}$.

density at $110 \mu\text{s}$ is still at its maximum value. As highlighted by the numerical results, cells 1 and 2 exhibit the maximum pore density in their central part directly facing the electrodes. In contrast, the pore density pertaining to the cell 3 is rather low due to its disadvantageous position with respect to the electrodes system. The developed modeling approach enables evaluation of the EP process on the whole three-dimensional geometry of the analyzed cell. In particular, it allows a global and more truthful analysis of the electroporation phenomenon taking into account the interinfluence of pore density on the whole cell membrane. Moreover, it does not treat cells as infinitely long “columns” which actually represent the 2D modeling [28], [29]. The intensity and duration of the applied electric field have typical values of the ECT treatment protocols, thus the analyzed cells are reversibly electroporated. Similarly, values relevant for IRE treatments can be obtained for the same cells by considering higher intensity values of the applied electric field experimentally, as well as numerically.

B. Exposure to HF-EP Pulses

Further simulations were carried out exposing the biological cells to a short unipolar pulse having a voltage amplitude of 60 V, duration $T_p = 1 \mu\text{s}$, delay time $T_d = 1 \mu\text{s}$, and rise and fall times of $0.1 \mu\text{s}$. In this case, the main spectral energy spreads in a frequency range 1 MHz wide and the dispersive effects due to the plasma membrane medium become important. This kind of pulse was not used experimentally, but we performed simulations to highlight the importance of using the dispersive membrane properties when $1 \mu\text{s}$ pulses are used. Toward this aim, the model including the frequency-dependent dielectric response was implemented, and a comparison between the dispersive and the non-dispersive models was carried out.

Figs. 9 and 10 report the temporal evolution of the induced TMV and pore density obtained using the dispersive (D) and non-dispersive (nD) models. The performed analysis shows a

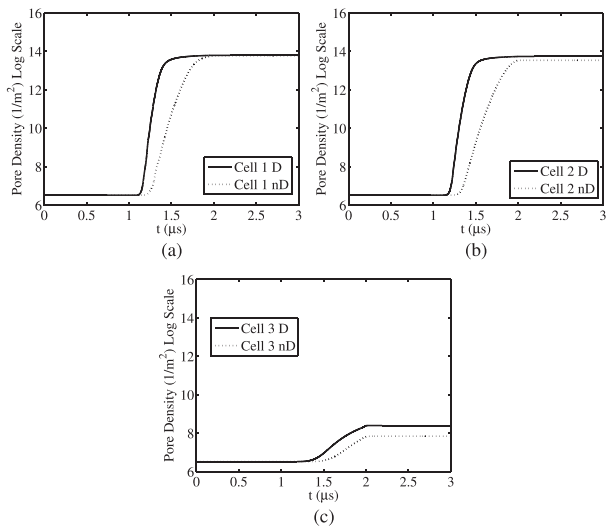


Fig. 10. Temporal evolution of pore density for (a) cell 1, (b) cell 2, and (c) cell 3 obtained using the dispersive (D) and non-dispersive (nD) model. Rectangular unipolar pulse type, voltage amplitude 60 V, pulse duration $T_p = 1 \mu\text{s}$, delay time $T_d = 1 \mu\text{s}$, rise time $t_r = 0.1 \mu\text{s}$, and fall time $t_f = 0.1 \mu\text{s}$.

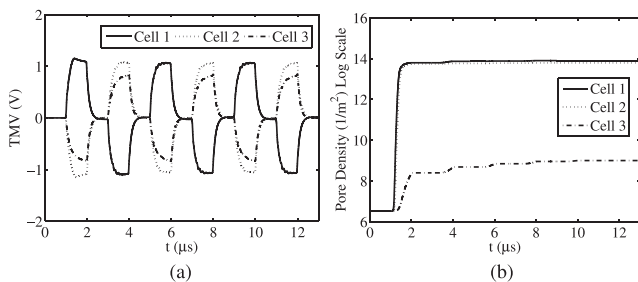


Fig. 11. Temporal evolution of (a) TMV and (b) pore density when three bipolar HF-EP pulses are applied. Each bipolar pulse has total duration, pulse width and delay between pulses are 3 μs , 1 μs , and 1 μs , respectively.

relevant difference between the two models. Indeed, the EP process is activated more quickly in the dispersive model than in the non-dispersive one. In fact, for cells 1 and 2 the EP activation occurs 0.1 μs faster with the dispersive than with the non-dispersive model. Furthermore, in the case of the non-dispersive model, the pore density is lower than that calculated using the dispersive one. In particular, Fig. 10 highlights that the relative error pertaining the regime value of the pore density is about 0.15%, 1.45%, and 6.6% (in a logarithmic scale) for cells 1, 2, and 3, respectively. As a result, the pore density values obtained using the dispersive and non-dispersive model are quite similar for cells 1 and 2, but differ significantly for cell 3. Thus, it can be concluded that for 1 μs pulses the dispersive electric properties should be taken into account.

To compare our calculations with the experimental data, a train of pulses composed of three bipolar HF-EP pulses was considered, too. In particular, with reference to one bipolar pulse, the total duration, pulse width, and delay between pulses are 3 μs , 1 μs , and 1 μs , respectively. Due to the short pulse duration, the dispersive numerical model was used to perform the simulations. Fig. 11(a) and 10(b) show the temporal evolution of the induced TMV and pore density calculated at the same plasma membrane

points as for the rectangular monopolar 100 μs long pulse. The numerical results infer that, with respect to the monopolar longer pulses (see Figs. 7(a) and 7(b)), the curves of TMV and the pore density strongly change in shape. As reported in Fig. 11(a), the TMV pertaining to cells 1 and 2 assume values between about -1 V and 1 V . Instead, for cell 3 the corresponding TMV approximately changes between -0.8 V and 0.8 V . As shown in Fig. 11(b), by applying a sequence of consecutive pulses, the pore density increases faster for cells 1 and 2. Moreover, each time a new HF-EP is applied, a small increase in pore density occurs. As highlighted by Fig. 11(b), the electroporation effects of the positive part of the electric pulse is not attenuated by its second negative part, thus not observing the so-called ‘‘pulse cancellation effect’’. As the reasons for the cancellation effect are not yet known, and it is not observed generally [30] that the cancellation effect cannot be reliably added to the model. As a result, each phase of the bipolar pulse determines an additive EP process. Also, in this case, it was determined that cells 1 and 2 are both electroporated, and cell 3 was not electroporated. So, the performed study confirms the possibility of using the bipolar pulses instead of the rectangular unipolar ones obtaining the same level of electroporation. Moreover, as reported in several *in vivo* studies, alleviation of muscle contractions is expected [31], [32].

C. The Drawbacks of Our Study

The calculations for the monopolar pulses were performed for one pulse, while in experiments we applied eight pulses. Similarly, in the HF-EP, the calculations were performed for three bipolar pulses, while in experiments eight bursts were used, each consisting of 50 bipolar pulses [7]. However, the implementation of the whole waveforms would require huge computational efforts and would be beyond the scope of the current study, as we want to place emphasis on the proof-of-principle that realistic and dispersive 3D cells. Moreover, we believe that actual microelectrodes systems should be used in the EP models.

In the simulation, the applied voltage was 60V for the monopolar and for the HF-EP bipolar pulses. We did not take into account the voltage drop along the electrodes, which decreases the applied voltage and cells ‘‘receive’’ less voltage than what is at the output of the generator. As our study served more as a proof-of-principle, the difference in the experimentally and numerically applied voltage did not influence our main findings on the agreement between experiments and simulations. The simulations were conducted using the same cells for both monopolar and HF-EP pulses, and the results of the simulations for both types of pulses were compared with the experimental results carried out using only the monopolar pulses. The presented model could be further extended by reconstructing the geometry of internal cellular structures, and it could also be used in the analysis of denser groups of cells.

V. CONCLUSION

In the study of the EP process of biological cells, an evaluation that is as close as possible to the reality of the temporal response and spatial distribution of the induced TMV and pore density is

of considerable importance. In this study, a non-linear dispersive numerical model was developed to evaluate the induced TMV and pore density along the plasma membranes of realistic 3D irregular cells when both long monopolar and HF-EP pulses are applied. In the 3D developed model, the Maxwell equations were solved in conjunction with the asymptotic Smoluchowski equation describing the pores creation and resealing. Furthermore, when the biological cells are exposed to HF-EP pulses, the dielectric dispersion of plasma membranes was modeled using a multi-relaxation Debye-based relationship. First, the biological cells were exposed to a rectangular monopolar pulse of 60 V, duration of 100 μ s, and rise and fall times of 0.1 μ s. By comparing the obtained numerical results with experimental ones, good agreement was obtained. To highlight the importance of considering the dispersive properties of the biological membrane, a comparison between the dispersive and the non-dispersive models was further carried out. The performed study highlights an important difference between the two models. In fact, the dispersive model shows faster initiation of the EP process and lower pore density values than the non-dispersive one. Adopting the dispersive model, further simulations were carried out, exposing biological cells to three HF-EP bipolar pulses. Therefore, the obtained numerical results were compared with the experimental ones carried out using the monopolar pulses. In conclusion, the performed numerical analysis shows a good agreement between the numerical and experimental results, and it highlights the possibility of using bipolar pulses to replace the unipolar rectangular pulse achieving a comparable level of electroporation.

ACKNOWLEDGMENT

The authors would like to thank M. Reberšek and E. Pirc at University of Ljubljana, for their help with the construction of the custom-made holder and the electrical measurements of the chamber resistance.

REFERENCES

- [1] T. Kotnik *et al.*, "Membrane electroporation and electropermeabilization: Mechanisms and models," *Ann. Rev. Biophys.*, vol. 6, no. 48, pp. 63–91, 2019.
- [2] M. L. Yarmush *et al.*, "Electroporation-based technologies for medicine: Principles, applications and challenges," *Annu. Rev. Biomed. Eng.*, vol. 16, pp. 295–320, 2014.
- [3] A. Sugrue *et al.*, "Irreversible electroporation for catheter-based cardiac ablation: A systematic review of the preclinical experience," *J. Interv. Card. Electrophysiol.*, vol. 55, no. 3, pp. 251–265, Sep. 2019.
- [4] J. J. Wendler *et al.*, "Angiography in the isolated perfused kidney: Radiological evaluation of vascular protection in tissue ablation by nonthermal irreversible electroporation," *Cardiovascular Interventional Radiol.*, vol. 35, no. 2, pp. 383–390, 2012.
- [5] C. B. Arena *et al.*, "High-frequency irreversible electroporation (H-FIRE) for non-thermal ablation without muscle contraction," *Biomed. Eng. Online*, vol. 10, no. 102, pp. 1–20, 2011.
- [6] T. Murovec *et al.*, "Modeling of transmembrane potential in realistic multicellular structures before electroporation," *Biophys. J.*, vol. 111, no. 10, pp. 2286–2295, 2016.
- [7] M. Scuderi *et al.*, "The use of high-frequency short bipolar pulses in cisplatin electrochemotherapy in vitro," *Radiol. Oncology*, vol. 53, no. 2, pp. 194–205, 2019.
- [8] E. Salimi, D. J. Thomson, and G. E. Bridges, "Membrane dielectric dispersion in nanosecond pulsed electroporation of biological cells," *IEEE Trans. Dielectr. Elect. Insul.*, vol. 20, no. 4, pp. 1256–1265, Aug. 2013.
- [9] K. C. Smith and J. C. Weaver, "Active mechanisms are needed to describe cell responses to submicrosecond, megavolt-per-meter pulses: Cell models for ultrashort pulses," *Biophys. J.*, vol. 95, no. 4, pp. 1547–1563, 2008.
- [10] G. Pucihar, D. Miklavčič, and T. Kotnik, "A time-dependent numerical model of transmembrane voltage induction and electroporation of irregularly shaped cells," *IEEE Trans. Biomed. Eng.*, vol. 56, no. 5, pp. 1491–1501, May 2009.
- [11] H. Qiu, S. Xiao, and R. P. Joshi, "Simulations of voltage transients across intracellular mitochondrial membranes due to nanosecond electrical pulses," *IEEE Trans. Plasma Sci.*, vol. 42, no. 10, pp. 3113–3120, Oct. 2014.
- [12] L. Mescia *et al.*, "Modeling of electroporation induced by pulsed electric fields in irregularly shaped cells," *IEEE Trans. Biomed. Eng.*, vol. 65, no. 2, pp. 414–423, Feb. 2018.
- [13] J. Dermol-Černe and D. Miklavčič, "From cell to tissue properties—Modeling skin electroporation with pore and local transport region formation," *IEEE Trans. Biomed. Eng.*, vol. 65, no. 2, pp. 458–468, Feb. 2018.
- [14] D. A. Stewart, T. R. Gowrishankar, and J. C. Weaver, "Transport lattice approach to describing cell electroporation: use of a local asymptotic model," *IEEE Trans. Plasma Sci.*, vol. 32, no. 4, pp. 1696–1708, Oct. 2004.
- [15] L. Towhidi *et al.*, "Variability of the minimal transmembrane voltage resulting in detectable membrane electroporation," *Electromagn. Biol. Med.*, vol. 27, no. 4, pp. 372–385, 2008.
- [16] G. Pucihar *et al.*, "Numerical determination of transmembrane voltage induced on irregularly shaped cells," *Ann. Biomed. Eng.*, vol. 34, no. 4, pp. 642–652, 2006.
- [17] Y. Zheng *et al.*, "Possible effects of electric fields on a pair of spherical cells," *J. Membrane Biol.*, vol. 250, no. 5, pp. 433–440, 2017.
- [18] L. Mescia *et al.*, "Design of electroporation process in irregularly shaped multicellular systems," *Electronics*, vol. 8, no. 37, pp. 1–17, 2019.
- [19] G. Pucihar, T. Kotnik, and D. Miklavčič, "An experimental and numerical study of the induced transmembrane voltage and electroporation on clusters of irregularly shaped cells," in *Proc. 11th Mediterranean Conf.*, 2007, pp. 639–642.
- [20] T. Y. Chang *et al.*, "Cell and protein compatibility of parylene-c surfaces," *Langmuir: ACS J. Surfaces Colloids*, vol. 23, no. 23, pp. 11 718–11 725, 2007.
- [21] H. Zou *et al.*, "Modification and characterisation of material hydrophobicity for surface acoustic wave driven microfluidics," in *Proc. IEEE Int. Conf. Microelectronic Test Struct.*, 2012, pp. 61–65.
- [22] P. P. Acharjya, R. Das, and D. Ghoshal, "Study and comparison of different edge detectors for image segmentation," *Global J. Comput. Sci. Technol. Graph. Vision*, vol. 12, no. 13, pp. 29–32, 2012.
- [23] L. Mescia *et al.*, "Fractional calculus based FDTD modeling of layered biological media exposure to wideband electromagnetic pulses," *Electronics*, vol. 6, no. 106, pp. 1–15, 2017.
- [24] M. A. Chiapperino *et al.*, "Nonlinear dispersive model of electroporation for irregular nucleated cells," *Bioelectromagnetics*, vol. 40, no. 5, pp. 331–342, 2019.
- [25] W. Krassowska and P. D. Filev, "Modeling electroporation in a single cell," *Biophys. J.*, vol. 92, pp. 404–417, 2007.
- [26] B. Klosgen *et al.*, "Dielectric spectroscopy as a sensor of membrane head-group mobility and hydration," *Biophys. J.*, vol. 71, no. 6, pp. 3251–3260, 1996.
- [27] L. Rems *et al.*, "Cell electrofusion using nanosecond electric pulses," *Scientific Rep.*, vol. 3, 2013, Art. no. 3382.
- [28] P. Lamberti *et al.*, "nsPEF-induced effects on cell membranes: Use of electrophysical model to optimize experimental design," *IEEE Trans. Dielectr. Elect. Insul.*, vol. 20, no. 4, pp. 1231–1238, Aug. 2013.
- [29] C. Merla *et al.*, "Microdosimetry for nanosecond pulsed electric field applications: A parametric study for a single cell," *IEEE Trans. Biomed. Eng.*, vol. 58, no. 5, pp. 1294–1302, May 2011.
- [30] T. Polajžer *et al.*, "Cancellation effect is present in high-frequency reversible and irreversible electroporation," *Bioelectrochemistry*, vol. 132, 2020, Art. no. 107442.
- [31] S. Dong *et al.*, "Parameters optimization of bipolar high frequency pulses on tissue ablation and inhibiting muscle contraction," *IEEE Trans. Dielectr. Elect. Insul.*, vol. 25, no. 1, pp. 207–216, Feb. 2018.
- [32] M. B. Sano *et al.*, "Reduction of muscle contractions during irreversible electroporation therapy using high-frequency bursts of alternating polarity pulses: A laboratory investigation in an ex vivo swine model," *J. Vascular Interventional Radiol.*, vol. 29, no. 6, pp. 893–898, 2019.